COMPLEX IMAGE SOLUTION OF SAR INSIDE A HUMAN HEAD ILLUMINATED BY A FINITE-LENGTH DIPOLE

A. A. Omar

Department of Electrical Engineering
King Faisal University
Al-Ahsa, Kingdom of Saudi Arabia

Abstract—This paper uses the accurate and computationally efficient complex image technique (CIT) to find the electric field and SAR distributions inside a human head illuminated by a finite-length dipole. The human head model used consists of 3 planar layers of lossy dielectrics. The accuracy of the results is verified by comparison with HFSS software. It was found that the CIT requires about 1 minute and 16 MB of RAM, while HFSS requires about 2 hours and 1.5 GB of RAM to find the SAR distribution using a 2.19 GHz Core 2 Due PC. The CIT method can also efficiently solve other types of antennas on other planar head models.

1. INTRODUCTION

The recent rapid spread of mobile phones has caused wide concern among the scientists and the public regarding the potential health hazard to the human head as a result of RF radiation from these phones. A parameter of great significance in determining the possibility of health hazard due to RF radiation inside a human head is the Specific Absorption Rate (SAR), which is defined as the power absorbed per unit mass of human tissue. Governments have put standards for the maximum SAR that should not be exceeded to avoid health hazards. This maximum is set to 1.6 W/kg averaged over 1 g of tissue, or 2 W/kg averaged over 10 g of tissue, in USA and Europe, respectively [1].

Several methods have been used to study the effect of an antenna radiator on a human head. These methods may be divided into two parts; 1) analytical and semi-analytical methods [2–17] based on idealized head geometry, such as homogenous or multilayered concentric spheres [2–14], eccentric spheres [15], multilayered planar model [16, 17], and 2) numerical methods dealing with complex head geometry. These numerical methods include the finite difference time domain (FDTD) [18–24] and the 3-D method of moments (MOM) [25]. In these methods, an anatomical human head is usually modeled based on magnetic resonance imaging (MRI). The analytical and semi-analytical methods are necessary for validation and assessment of the numerical techniques [13, 14].

In this paper, a semi-analytical method based on the complex image techniques (CIT) is used to find the SAR inside a human head modeled as three planar layers of lossy dielectrics. The use of planar layers as opposed to spherical layers was shown in [17] to have little effect on the SAR. In addition, several numerical experiments conducted, as part of this work, using commercial software, have shown that the maximum difference in SAR between our 3-layered planar model and a corresponding 3-layered spherical model does not exceed 10%. However, the use of a planar model simplifies formulations and allows for the implementation of the accurate and computationally efficient CIT [26–32].

The electric field inside the human head is obtained from the mixed potential complex image Green's functions when the source is a dipole antenna of finite length. Consequently, the SAR in the three layers ($i = 1, 2, 3$) is obtained from the E-field using the following formula:

$$\mathrm{SAR}_i = \frac{P_i}{\rho_i} = \frac{|E_i|^2 \sigma_i}{2\rho_i}$$

where P_i is the dissipated power density in the ith layer in W/m^3, ρ_i is the mass density in (kg/m^3), σ_i is the conductivity of the ith layer in (S/m), and $|E_i|$ is the magnitude of the electric field of the ith layer in (V/m). SAR has units of W/kg.

The CIT is used to convert the mixed potentials from the spectral domain to the space domain without performing the time consuming numerical integration of Sommerfeld's integrals [26]. This yields better than 10 fold reduction in computation time without sacrificing the accuracy [26]. The CIT relies on extracting the quasi-dynamic (low frequency) part of the Green's function, and then expanding the rest of the spectral function in terms of a finite number of complex exponentials using Prony's method [33]. These complex exponentials are converted to the space domain analytically using the Sommerfeld's

identity [34]. This results in a set of real images representing the quasi-dynamic contribution, and a set of complex images representing the radiation and surface waves. The resultant complex images are only a few images with complex amplitudes and complex locations. While the CIT is applied in this paper to solve a three-layer model of the human head, it can be easily extended to other head models consisting of any number of planar layers with different types of conductor or slot antennas [26–32].

Section 2 describes the multi-layered structure of the human head used in this paper, and provides the parameters of the different layers. Section 3 provides the spectral domain expressions of the mixed potentials in the three layers. Section 4 explains the complex image technique for converting the mixed potentials from the spectral domain to the space domain. Section 5 explains how the E-field is obtained from the mixed potentials. Section 6 provides results that show the validity and accuracy of our Green's functions and SAR. Section 7 provides our conclusions.

2. THREE-LAYERED MODEL OF THE HUMAN HEAD

In this paper, the model used for the human head consists of three planar layers of lossy dielectrics, as shown in Fig. 1. The dielectric constant, conductivity, and mass density of the three layers are shown in Table 1 at 900 MHz and 1800 MHz [5]. The radiating antenna is a finite length dipole, as shown in Fig. 1.
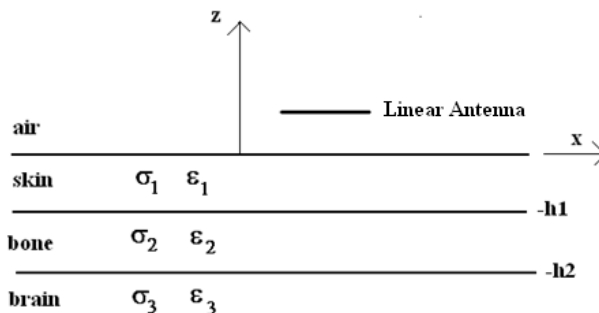
Figure 1. Geometry of the problem showing the human head model and the radiating antenna ($h_1 = 5$ mm, $h_2 = 10$ mm).

Table 1. The parameters of the layers of Fig. 1 at 900 MHz and 1.8 GHz [5].

Material	900 MHz		1.8 GHz		Mass density (kg/m³)
	ϵ_r	σ (S/m)	ϵ_r	σ (S/m)	
Skin	39.5	0.7	38.2	0.9	1080
Bone	12.5	0.17	12	0.29	1180
Brain	56.8	1.1	51.8	1.5	1050

3. GREEN'S FUNCTION FOR THE MAGNETIC VECTOR POTENTIAL $\tilde{G}_{Axx}$ AND ELECTRIC SCALAR POTENTIAL $\tilde{G}_q$ IN THE SPECTRAL DOMAIN

The finite length dipole is divided into an infinite number of Hertzian dipoles located at height $z = z'$ in the air region. The spectral domain mixed potential Green's functions in layer i due to the Hertzian dipole are obtained from the transmission coefficient of the TE_z wave (T_{TEi}) and the transmission coefficient of the TM_z wave (T_{TMi}), taken from the source plane at $z = z'$ to the field plane at $z = z$ in ith layer. These Green's functions are given in general by:

$$\tilde{G}_{Axx,i}(z, z') = \frac{\mu_o}{j2k_{zo}} T_{TEi} \tag{1}$$

$$G_{q,i}(z, z') = \frac{1}{j2\left(\epsilon_{ri} - \frac{j\sigma_i}{\omega\epsilon_o}\right)k_{zo}}\left[T_{TEi} + \frac{k_{zi}^2}{k_\rho^2}\left(T_{TEi} - \frac{k_{zo}}{jk_{zi}^2}\frac{\partial T_{TMi}}{\partial z}\right)\right] \tag{2}$$

where ϵ_{ri} and σ_i are the dielectric constant and conductivity in layer i, where $i = 0, 1, 2, 3$ correspond to the air, skin, bone, and brain layers, respectively, and k_{zi} is the wave-number in the ith layer.

The transmission coefficients T_{TEi} and T_{TMi} in the ith layer are obtained using the wave matrix technique [35]. The expressions of these coefficients in each layer are given by:

3.1. In the Air Region (Layer 0) where $z \geq 0$

$$T_{TEo} = e^{-jk_{zo}(z'-z)} + R_{TE}e^{-jk_{zo}(z'+z)} \tag{3}$$

$$R_{TE} = \frac{\begin{array}{l} r_{o1}^{TE} + r_{12}^{TE}e^{-j2k_{z1}h_1} + r_{o1}^{TE}r_{12}^{TE}r_{23}^{TE}e^{j2k_{z2}(h_1-h_2)} \\ +r_{23}^{TE}e^{-j2[k_{z1}h_1+k_{z2}(h_2-h_1)]} \end{array}}{\begin{array}{l} 1 + r_{o1}^{TE}r_{12}^{TE}e^{-j2k_{z1}h_1} + r_{12}^{TE}r_{23}^{TE}e^{j2k_{z2}(h_1-h_2)} \\ +r_{o1}^{TE}r_{23}^{TE}e^{-j2[k_{z1}h_1+k_{z2}(h_2-h_1)]} \end{array}} \tag{4}$$

T_{TMo} is obtained from T_{TEo} by replacing every E with M in Equations (3) and (4), and

$$r_{ij}^{TE} = \frac{k_{zi} - k_{zj}}{k_{zi} + k_{zj}} \tag{5}$$

$$r_{ij}^{TM} = \frac{\left(\epsilon_{rj} - \frac{j\sigma_j}{\omega\epsilon_o}\right) k_{zi} - \left(\epsilon_{ri} - \frac{j\sigma_i}{\omega\epsilon_o}\right) k_{zj}}{\left(\epsilon_{rj} - \frac{j\sigma_j}{\omega\epsilon_o}\right) k_{zi} + \left(\epsilon_{ri} - \frac{j\sigma_i}{\omega\epsilon_o}\right) k_{zj}} \tag{6}$$

$$k_{zi}^2 + k_\rho^2 = k_o^2 \left(\epsilon_{ri} - \frac{j\sigma_i}{\omega\epsilon_o}\right) \tag{7}$$

where k_ρ is the wavenumber in the radial direction (in x-y plane) and is given by $k_\rho = \sqrt{k_x^2 + k_y^2}$ [27].

3.2. In the Skin Layer (Layer 1) where $-h_1 \leq z < 0$

$$T_{TE1} = \frac{\left(1 + r_{o1}^{TE}\right) \left[Y_E + X_E e^{-j2k_{z1}(z+h_1)}\right]}{\left(Y_E + X_E r_{o1}^{TE} e^{-j2k_{z1}h_1}\right)} e^{-jk_{zo}z'} e^{jk_{z1}z} \tag{8}$$

$$X_E = r_{12}^{TE} + r_{23}^{TE} e^{-j2k_{z2}(h_2-h_1)} \tag{9}$$

$$Y_E = 1 + r_{12}^{TE} r_{23}^{TE} e^{-j2k_{z2}(h_2-h_1)} \tag{10}$$

T_{TM1} is obtained from T_{TE1} by replacing every E with M in Equations (8)–(10).

3.3. In the Bone Layer (Layer 2) where $-h_2 \leq z < -h_1$

$$T_{TE2} = \frac{\left(1 + r_{o1}^{TE}\right) \left(1 + r_{12}^{TE}\right) \left(1 + r_{23}^{TE} e^{-j2k_{z2}(h_2+z)}\right)}{D_E} e^{-jk_{zo}z'} \tag{11}$$

$$\begin{aligned} D_E = {} & e^{j(k_{z1}h_1 - k_{z2}(h_1+z))} + r_{o1}^{TE} r_{12}^{TE} e^{-j(k_{z1}h_1 + k_{z2}(h_1+z))} \\ & + r_{12}^{TE} r_{23}^{TE} e^{j(k_{z1}h_1 + k_{z2}(h_1+z) - 2k_{z2}(h_2+z))} \\ & + r_{o1}^{TE} r_{23}^{TE} e^{-j(k_{z1}h_1 - k_{z2}(h_1+z) + 2k_{z2}(h_2+z))} \end{aligned} \tag{12}$$

T_{TM2} is obtained from T_{TE2} by replacing every E with M in Equations (11) and (12).

3.4. In the Brain Layer (Layer 3) where $z \leq -h_2$

$$T_{TE3} = \frac{\left(1 + r_{o1}^{TE}\right)\left(1 + r_{12}^{TE}\right)\left(1 + r_{23}^{TE}\right)}{D_G} e^{-jk_{zo}z'} \tag{13}$$

$$
\begin{aligned}
D_G = \; & e^{j(k_{z1}h_1 + k_{z2}(h_2 - h_1) - k_{z3}(h_2 + z))} \\
& + r_{o1}^{TE} r_{12}^{TE} e^{j(-k_{z1}h_1 + k_{z2}(h_2 - h_1) - k_{z3}(h_2 + z))} \\
& + r_{12}^{TE} r_{23}^{TE} e^{j(k_{z1}h_1 + k_{z2}(h_1 - h_2) - k_{z3}(h_2 + z))} \\
& + r_{o1}^{TE} r_{23}^{TE} e^{j(-k_{z1}h_1 - k_{z2}(h_2 - h_1) - k_{z3}(h_2 + z))}
\end{aligned} \tag{14}
$$

T_{TM3} is obtained from T_{TE3} by replacing every E with M in Equations (13) and (14).

4. COMPLEX IMAGE GREEN'S FUNCTIONS

The next step is to convert the Green's function in (1) and (2) from the spectral domain to the space domain. For this purpose the well known Sommerfeld integrals [35] are performed. These integrals have the following general form:

$$G(\rho, z, z') = \frac{1}{4\pi} \int_{-\infty}^{\infty} \tilde{G}(k_\rho, z, z') H_o^2(k_\rho \rho) k_\rho dk_\rho \tag{15}$$

where $\tilde{G} = \tilde{G}_{Axx,i}$ or $\tilde{G}_{q,i}$. The Sommerfeld's integral in (15) is time consuming due to the oscillatory nature of the integrand and the possibility of surface wave poles. In this paper, the complex image technique [27] (CIT) is used to avoid the numerical integration of Sommerfeld's integral and perform the integration analytically.

The first step in the CIT is to extract the quasi-dynamic (i.e., low frequency) contribution from the integrand whose general form is shown in (15). At very low frequencies, the following approximations hold:

$$k_{zo} \cong k_{z1} \cong k_{z2} \cong k_{z3} \tag{16}$$

Appling the approximations in (16) to the Equations (1) and (2), results in the spectral domain quasi-dynamic part of the Green's functions. This part can be converted analytically to the space domain using the Sommerfeld identity given by:

$$\frac{e^{-jk_o r_o}}{r_o} = \int_{-\infty}^{\infty} \frac{1}{j2k_{zo}} e^{jk_{zo}(z - z')} H_o^2(k_\rho \rho) k_\rho dk_\rho \tag{17}$$

where

$$r_o = \sqrt{\rho^2 + (z - z')^2} \tag{18}$$

To avoid repetition, we only show how the CIT is used to convert the Green's function $\tilde{G}_{Axx,o}$ from the spectral domain to the space domain. The conversion of the Green's functions in the other layers is similar.

The space domain Green's function $\tilde{G}_{Axx,o}$ in layer 0 is expressed as:

$$G_{Axx,0} = G_{A,qu,o} + G_{A,ci,o} \tag{19}$$

where $G_{A,qu,o}$ and $G_{A,ci,o}$ are the quasi-dynamic and complex image parts of the Green's function in region 0. They are given by:

$$G_{A,qu,o} = \frac{\mu_o}{4\pi} \frac{e^{-jk_o r_o}}{r_o} \tag{20}$$

$$G_{A,ci,o} = \frac{\mu_o}{4\pi} \int_{-\infty}^{\infty} \frac{1}{j2k_{zo}} R_{TE} e^{-jkzo(z'+z)} H_o^2(k_\rho \rho) k_\rho dk_\rho \tag{21}$$

where R_{TE} is given in (4).

The above integration in (21) can be performed along the real axis C_o in the complex k_ρ-plane, or a long a deformed path C_1 passing through the origin and lying in the first and third quadrants, as shown in Fig. 2. This deformation can be achieved because no singularity is encountered in the deformation. The parametric equation for the path C_1 in the complex k_{zo}-plane is given by [27]:

$$C_1: \quad k_{zo} = k_o \left[-jt + \left(1 - \frac{t}{T_o} \right) \right]; \quad 0 \le t \le T_o \tag{22}$$

where T_o is the truncation point used to replace infinity in the integrations.
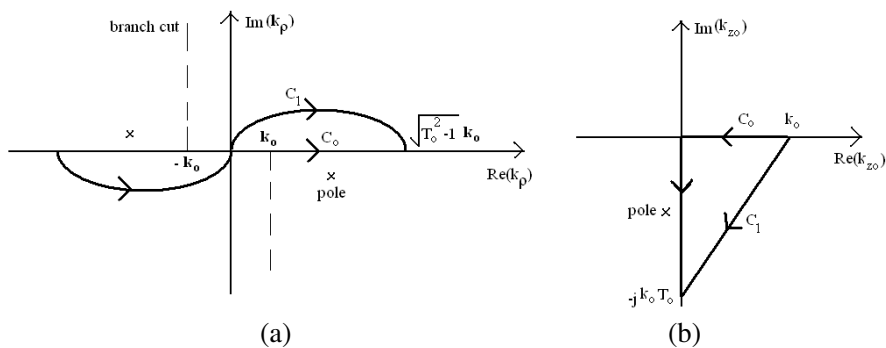
Figure 2. (a) The integration contours C_o and C_1 in the complex k_ρ-plane. (b) The integration contours C_o and C_1 in the complex k_{zo}-plane.

The next step in the CIT is to use Prony's method [33] to approximate the spectral function R_{TE} in (21) as a finite sum of exponentials in the complex variable k_{zo} along the deformed path C_1, i.e.,

$$R_{TE} = \sum_{i=1}^{N} a_i e^{jb_i k_{zo}/k_o} \tag{23}$$

Substituting (23) in (21) and using the Sommerfeld identity in (17), results in the following complex image part of the Green's function:

$$G_{A,ci,o} = \frac{\mu_o}{4\pi} \sum_{i=1}^{N} a_i \frac{e^{-jk_o r_i}}{r_i} \tag{24}$$

where

$$r_i = \sqrt{\rho^2 + \left(z + z' - \frac{b_i}{k_o}\right)^2} \tag{25}$$

In summary, each Green's function is expressed using CIT in terms of a set of real images (quasi-dynamic part) which have real amplitudes and real locations, and another set of complex images which have complex amplitudes and complex locations. The number of complex images is denoted by N. In this work, there is no need to extract the surface wave poles because we are mainly interested in the human head region under the dipole where the SAR is maximum (i.e., for small radial distance ρ) [27]. The verification of the accuracy of the complex images Green's functions is given in Section 6.1.

5. THE *E*-FIELD IN TERMS OF THE MIXED POTENTIALS

The *E*-field in layer i, due to a finite length dipole of length L placed along the *x*-axis at location $z = z'$, as shown in Fig. 1, is given by:

$$E_{x,i}(\rho, z) = \int_{-L/2}^{L/2} \left(-j\omega G_{Axx,i} + \frac{1}{j\omega}\frac{\partial^2}{\partial x^2}G_{q,i}\right) I(x')dx' \tag{26}$$

where $I(x')$ is the current on the linear antenna which is assumed sinusoidal to simplify the formulation since dipole radius is assumed much smaller than wavelength. It is given by [36]:

$$I(x') = I_o \sin\left[k_o\left(\frac{L}{2} - |x'|\right)\right] \tag{27}$$

where I_o is the feed current.

The other field components are given by:

$$E_{z,i} = \int_{-L/2}^{L/2} G_{Ezx,i} I(x')\,dx' \tag{28}$$

where

$$G_{Ezx,i} = \frac{1}{4j\omega\varepsilon_o} \frac{\partial^2}{\partial x \partial z} \sum_{i=1}^{N} c_i \frac{e^{-jk_o r'_i}}{r'_i} \tag{29}$$

$$E_{y,i} = \int_{-L/2}^{L/2} G_{Eyx,i} I\left(x'\right) dx' \tag{30}$$

where

$$G_{Eyx,i} = \frac{4\left(x - x'\right)\left(y - y'\right)}{4\pi j\omega\epsilon_o\epsilon_{ri}}$$
$$\left\{ e^{-jk_o r_o} \left(\frac{3jk_o}{4r_o^4} - \frac{k_o^2}{4r_o^3} + \frac{3}{4r_o^5}\right) + \sum_{i=1}^{N} c_i e^{-jk_o r'_i} \left(\frac{3jk_o}{4r'^4_i} - \frac{k_o^2}{4r'^3_i} + \frac{3}{4r'^5_i}\right) \right\} \tag{31}$$

where c_i and r'_i result from the Prony approximation of T_{TMi}, and r_o is given in (18).

6. RESULTS AND DISCUSSION

6.1. Verification of the Accuracy of the Complex Image Green's Functions

To verify the accuracy of the complex image Green's functions in the different layers, Fig. 3 shows the Green's function for the electric
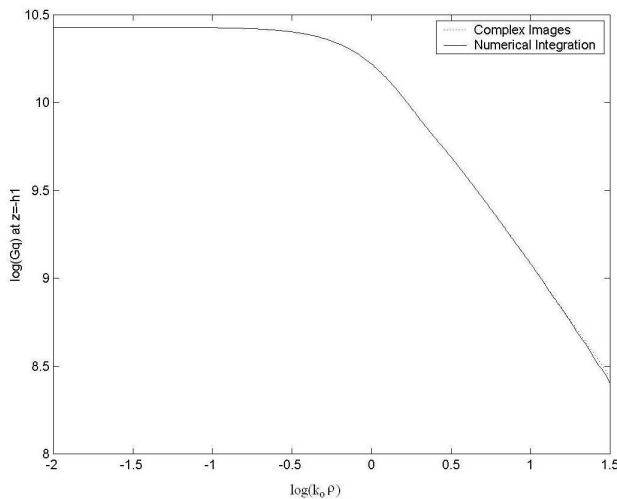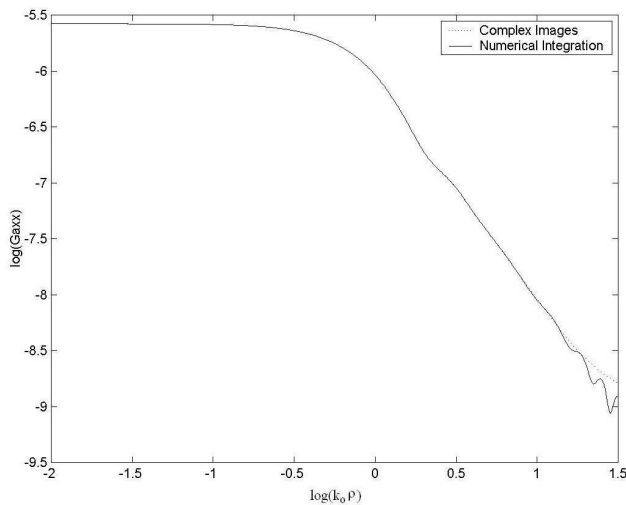

Figure 3. Comparison between G_q at $z = -h_1$ obtained using CIT and numerically for the layered medium of Fig. 1 ($N = 10$, $T_o = 10$, $z' = 2\,\mathrm{cm}$).

scalar potential G_q obtained using CIT at the interface $z = -h_1$, as compared to the corresponding Green's function obtained by numerically integrating Sommerfeld's integral (Eq. (15)). Excellent agreement is obtained. The CIT Green's function for the magnetic vector potential G_{Axx} at the interface $z = 0$ is also obtained and found to have excellent agreement with the corresponding Green's function obtained by the numerical integration of Sommerfeld's integrals, as shown in Fig. 4.

6.2. *E*-field and SAR Calculation

Results are also obtained for the local SAR distribution inside the human head, and compared with results obtained using the finite element software HFSS [37] at frequencies of 1800 MHz and 900 MHz. The agreement is very good, as shown in Figs. 5 and 6, respectively. The antenna used in this figure is a half wave dipole placed at a distance of 2 cm from the head.

To investigate the effect of antenna-head spacing, results are obtained using CIT for the maximum local SAR as a function of antenna-head spacing, as shown in Fig. 7. The radiating antenna is a half wavelength dipole at 1.8 GHz. It can be observed that SAR drops with increasing antenna-head spacing almost quadratically.


Figure 4. Comparison between G_{Axx} at $z = 0$ obtained using CIT and numerically for the layered medium of Fig. 1 ($N = 10$, $T_o = 10$, $z' = 2.$ cm).
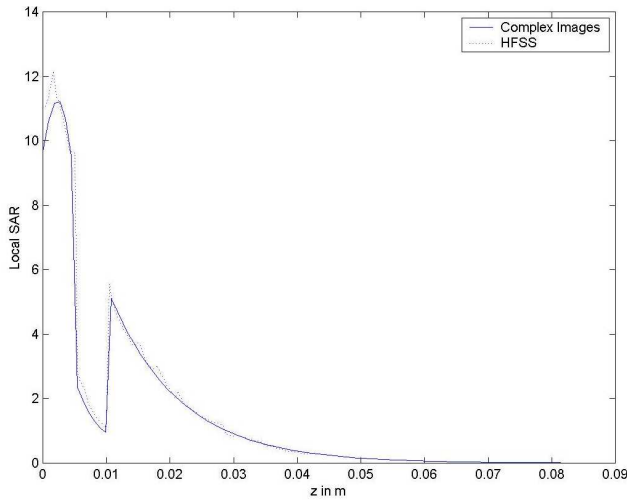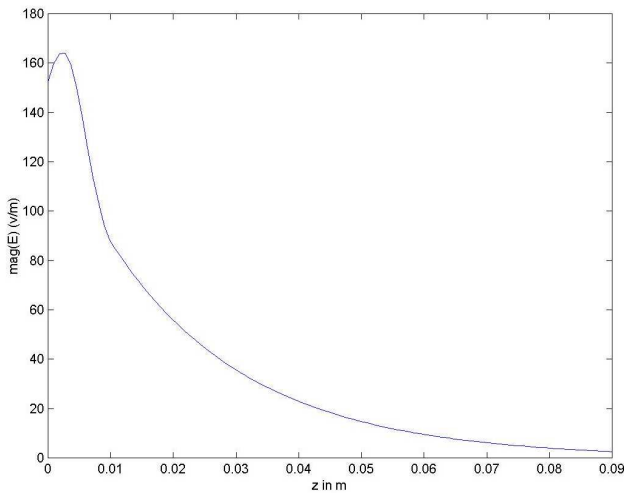
Figure 5. The local SAR distribution along the z-axis inside a human head for a dipole at a height of $2 \, \text{cm}$ above the head surface, $I_o = 165.5 \, \text{mA}$, $f = 1800 \, \text{MHz}$.
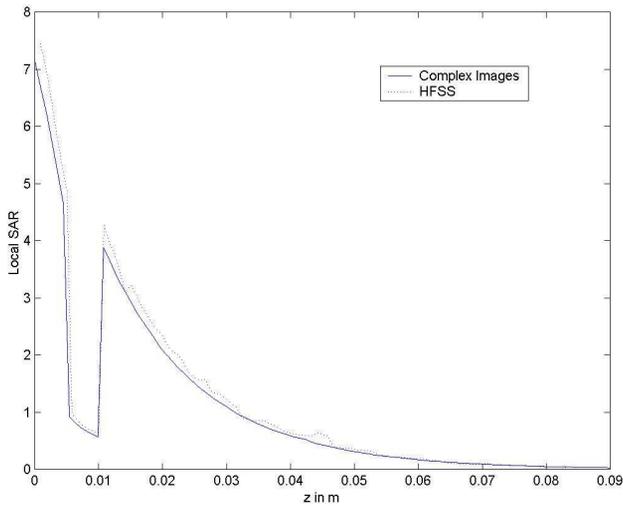

Figure 6. The local SAR distribution along the z-axis inside a human head for a dipole at a height of $2 \, \text{cm}$ above the head surface, $I_o = 165.5 \, \text{mA}$, $f = 900 \, \text{MHz}$.
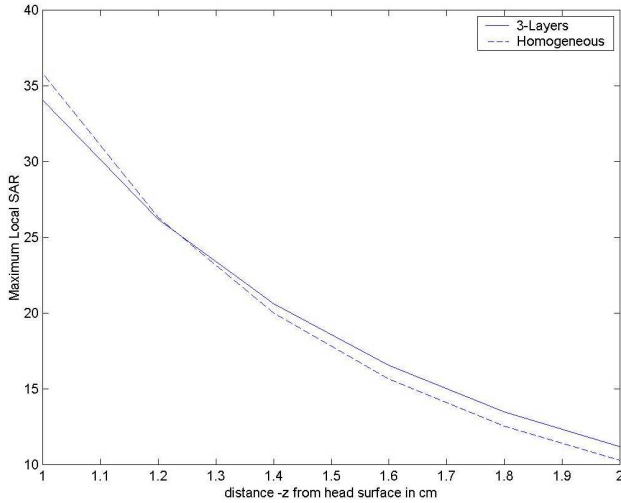
Figure 7. The maximum local SAR along the z-axis inside a human head as a function of antenna-head spacing for a 3-layered head model and a homogeneous head model. $I_o = 165.5\,\text{mA}$, $f = 1.8\,\text{GHz}$.

Figure 8. Electric field distribution along the z-axis inside a human head at $f = 1.8\,\text{GHz}$. The antenna is a half wavelength placed 2 cm away from the head surface, $I_o = 165.5\,\text{mA}$.
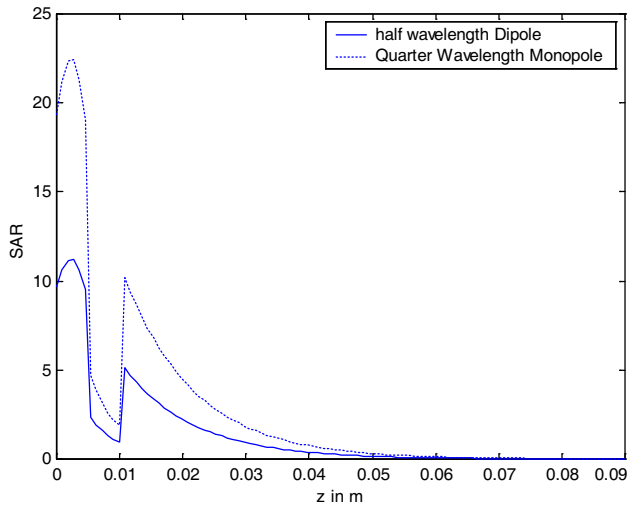
Figure 9. SAR distribution inside a human dead illuminated by a half wavelength dipole and a quarter wavelength monopole placed 2 cm from the human head at 1.8 GHz.

Our numerical investigations have shown that the number of layers in the human head model has little effect on the maximum local SAR. To demonstrate this, we obtained the SAR assuming the human head to be homogeneous (brain material only) and compared it with the 3 layers case. The difference is very small, as shown in Fig. 7.

The electric field distribution inside the human head along the z-axis is also obtained and shown in Fig. 8.

The effect of frequency on SAR is also investigated. Examining Figs. 5 and 6 clearly indicates that SAR increases with increasing frequency, because as the frequency is increased, the skin depth is decreased causing an increase in dissipated power.

The SAR distributions for a half wavelength dipole and a quarter wavelength monopole antennas placed 2 cm from the human head are shown in Fig. 9. This figure shows that SAR of a monopole is about double that of a dipole assuming that they radiate the same power.

7. CONCLUSION

The complex image technique (CIT) is applied in this paper to solve for the E-field and SAR distributions inside a human head modeled as 3 layers of planar lossy dielectric tissues. The CIT avoids the time consuming numerical integration of Sommerfeld's integrals without

sacrificing the accuracy. The accuracy of the complex image Green's functions is verified through several comparisons with the numerical integration of Sommerfeld's integrals. In addition, the accuracy of our results for the SAR is verified through comparisons with HFSS. From the computations point of view, the CIT requires about 1 minute and 16 MB of RAM, while HFSS requires about 2 hours (using version 9) and 1.5 GB of RAM on a Core-2-Due computer to produce the same SAR distribution along the z-axis inside the human head.

REFERENCES

1. International Commission on Non-Ionizing Radiation Protection (ICNIRP), "Guidelines for limiting exposure to time-varying electric, magnetic, and electromagnetic fields (up to 300 GHz)," *Health Physics*, Vol. 74, No. 4, 494–522, Apr. 1998.

2. Cerrio, G., R. DeLeo, and G. Rosellini, "Evaluation of electromagnetic power deposition in a spherical multilayer head in the near field of a linear antenna," *Wireless Netw.*, Vol. 3, 499–510, 1997.

3. Kriticos, H. N. and H. P. Schwan, "Formation of hot spots in multilayered spheres," *IEEE Trans. Biomed. Eng.*, Vol. 23, No. 2, 168–172, Mar. 1976.

4. Cottis, P. G. and N. K. Uzunoglu, "Focusing properties of dipole arrays placed near a multilayer lossy sphere," *Journal of Electromagnetic Waves and Applications*, Vol. 4, No. 5, 431–440, 1990.

5. Khalatbari, S., D. Sardari, A. Mirzaee, and H. Sadafi, "Calculating SAR in two models of the human head exposed to mobile phones radiations at 900 and 1800 MHz," *PIERS Online*, Vol. 2, No. 1, 104–109, 2006.

6. Wait, J. R., "On the electromagnetic response of a conducting sphere to a dipole field," *Geophyz.*, Vol. 25, No. 3, 649–658, Jun. 1960.

7. Kriticos, H. N. and H. P. Schwan, "Hot spots generated in conducting spheres by electromagnetic waves and biological implications," *IEEE Trans. Biomed. Eng.*, Vol. 19, 53–58, 1972.

8. Joines, W. T. and R. J. Spiegel, "Resonance absorption of microwaves by the human skull," *IEEE Trans. Biomed. Eng.*, Vol. 21, 46–48, Jan. 1974.

9. Weil, C. M., "Absorption characteristics of multilayered sphere models exposed to UHF/microwave radiation," *IEEE Trans. Biomed. Eng.*, Vol. 22, 468–476, Nov. 1975.

10. Iskander, M. F., P. W. Barber, C. H. Dumev, and H. Massoudi, "Irradiation of prolate spheroidal models of humans in the near field of a short electric dipole," *IEEE Trans. Microwave Theory Tech.*, Vol. 28, 801–807, Jul. 1980.

11. Uzunoglu, N. K. and E. A. Angelikas, "Field distributions in a three-layer prolate spheriodal human body model for a loop antenna irradiation," *IEEE Trans. Antennas Propagat.*, Vol. 35, 1180–1185, Oct. 1987.

12. Li, L., P. Kooi, M. S. Leong, and T. S. Yeo, "Electromagnetic dyadic Green's function in spherically multilayered media," *IEEE Trans. Microwave Theory Tech.*, Vol. 42, 2302–2309, Dec. 1994.

13. Nikita, K. S., G. S. Stamatakos, N. K. Uzunoglu, and A. Karafotias, "Analysis of the interaction between a layered spherical human head model and a finite-length dipole," *IEEE Trans. on Microwave Theory and Tech.*, Vol. 48, No. 11, 2003–2013, 2000.

14. Khodabakhshi, H. and A. Cheldavi, "Irradiation of a six-layered spherical model of human head in the near field of a half-wave dipole antenna," *IEEE Trans. on Microwave Theory and Tech.*, Vol. 58, No. 3, 680–690, 2010.

15. Skaropoulos, N. C., M. P. Ioannidou, and D. P. Chrissoulidis, "Induced EM field in a layered eccentric spheres model of the head: Plane-wave and localized source exposure," *IEEE Trans. Microwave Theory Tech.*, Vol. 44, 1963–1973, Oct. 1996.

16. Akram, A. and T. Andrew, "A multi layered model of human head irradiated by electromagnetic plane wave of 100 MHz–300 GHz," *Int. J. Sci. Res.*, Vol. 15, 2005.

17. Omar, A. A., Q. M. Bashayreh, and A. M. Al-Shamali, "Investigation of the effect of obliquely incident plane wave on a human head at 900 MHz and 1800 MHz," *Int. Journal of RF and Microwave Computer Aided Engineering (RFMICAE)*, Vol. 20, No. 2, 133–140, 2010.

18. Gandhi, O. P. and J. Y. Chen, "Electromagnetic absorption in the human head from experimental 6-GHz handheld transceivers," *IEEE Trans. Electromagn. Compat.*, Vol. 37, No. 4, 547–558, Apr. 1985.

19. Dimbylow, P. J. and O. P. Gandhi, "Finite-difference time-domain calculation of SAR in a realistic heterogeneous model of the head for plane-wave exposure from 600 MHz to 3 GHz," *Phys. Med. Biol.*, Vol. 36, No. 8, 1075–1089, 1991.

20. Okoniewski, M. and M. A. Stuchly, "A study of the handset antenna and human body interaction," *IEEE Trans. Microwave*

Theory and Tech., Vol. 44, No. 10, 1855–1864, Oct. 1995.

21. Jensen, A. and Y. Rahmat-Samii, "EM interaction of handset antennas and a human in personal communications," *Proc. IEEE*, Vol. 83, No. 1, 7–17, Jan. 1995.

22. Dimbylow, P. J. and S. M. Mann, "SAR calculations in an anatomically realistic model of the head for mobile communication transceivers at 900 MHz and 1.8 GHz," *Phys. Med. Biol.*, Vol. 39, No. 9, 1537–1553, 1994.

23. Makris, N., N. Angelone, S. Tulloch, S. Sorg, J. Kaiser, D. Kenedy, and G. Bonmassar, "MRI based anatomical model of the human head for specific absorption rate mapping," *Med. Biol. Eng. Comput.*, Vol. 46, 1239–1251, 2008.

24. Christ, A., A. Klingenbock, T. Samaras, C. Goiceanu, and N. Koster, "The dependence of electromagnetic far field absorption on body tissue composition in the frequency range from 300 MHz to 6 GHz," *IEEE Trans. Microwave Theory Tech.*, Vol. 54, No. 5, 2188–2195, May 2006.

25. Chuang, H. R., "Human operator coupling effects on radiation characteristics of a portable communications dipole antenna," *IEEE Trans. Antenna Propag.*, Vol. 42, No. 4, 556–560, Apr. 1994.

26. Chow, Y. L., J. J. Yang, D. G. Fang, and G. E. Howard, "A closed-form spatial Green's function for the thick microstrip substrate," *IEEE Trans. on Microwave Theory and Tech.*, Vol. 39, No. 3, 558–592, 1991.

27. Yang, J. J. and Y. L. Chow, "Discrete complex images of a three-dimesnional dipole above and within a lossy ground," *IEE Proc.*, Part H., Vol. 138, No. 4, 319–326, 1991.

28. Yang, J. J., Y. L. Chow, G. E. Howard, and D. G. Fang, "Complex images of an electric dipole in homogeneous and layered dielectrics between two ground planes," *IEEE Trans. Microwave Theory Tech.*, Vol. 40, No. 3, 595–600, Mar. 1992.

29. Hojjat, N., S. Safavi-Naeini, and Y. L. Chow, "Numerical computation of complex image Green's functions for multilayer dielectric media: Near field zone and the interface region," *IEEE Proc. Microwave, Antennas and Propagation*, Vol. 145, No. 6, 449–454, Dec. 1998.

30. Ling, F. and J.-M. Jin, "Discrete complex image method for Green's functions of general multilayer media," *IEEE Microwave and Guided Wave Lett.*, Vol. 10, No. 10, 400–402, Oct. 2000.

31. Yuan, M., T. K. Sarkar, and M. Salazar-Palma, "A direct discrete complex image method from the closed-form Green's functions

in multilayered media," *IEEE Trans. Microwave Theory Tech.*, Vol. 54, No. 3, 1025–1032, Mar. 2006.

32. Yuan, M., Y. Zhang, Z. Ji, and T. K. Sarkar, "Two-dimensional discrete complex image method (DCIM) for closed-form Green's function of arbitrary 3-D structures in general multilayered media," *IEEE Trans. Antennas and Propagat.*, Vol. 56, No. 5, 1350–1357, May 2008.

33. Hamming, R. W., *Numerical Methods for Scientists and Engineers*, Dover, New York, 620–622, 1973.

34. Stratton, J. A., *Electromagnetic Theory*, McGraw Hill, New York, 576, 1941.

35. Kong, J. A., *Electromagnetic Wave Theory*, Ch. 3, John Wiley & Sons, Inc., New York, 1990.

36. Elliott, R. S., *Antenna Theory and Design*, IEEE Computer Society Press, 2003.

37. Ansoft HFSS, Version 9, of Ansoft Inc.